Chapter 2
Hybrid Optical–Electrical Brain Computer Interfaces, Practices and Possibilities

Tomas E. Ward

2.1 Introduction

In this chapter we present an overview of the area of electroencephalography-functional near infrared spectroscopy (EEG-fNIRS) measurement as an activity monitoring technology for brain computer interfacing applications. Our interest in this compound neural interfacing technology is motivated by a need for a motor cortical conditioning technology suitable for use in a neurorehabilitation setting [15, 50]. Specifically we seek BCI technology that allows a patient with a paretic limb (as a consequence of stroke) to engage in movement-based rehabilitation exercises which will, we hope, encourage neuroplastic processes in the brain so that recovery and function is ultimately restored [38]. As we are interested in rehabilitation following stroke haemodynamic signatures of motor cortical activity coupled with the corresponding direct measures of the electrical activity of the neurons involved could be a rich source of new information on the recovering brain areas. While most neural engineers will be familiar with the concepts underpinning the electroencephalogram (EEG), the same cannot be said for fNIRS. Consequently this chapter will discuss much of the foundational concepts underlying this measurement before describing an EEG-fNIRS probe and early experiments which illustrate the concept and highlight aspects of the utility of this hybrid BCI approach.

2.2 The Underlying Physiological Origins of EEG and fNIRS

It is appropriate at this juncture to consider the physical basis of the measurements generated during both electroencephalography and fNIRS. While both measurement

T.E. Ward (✉)
Department of Electronic Engineering, National University of Ireland Maynooth, Maynooth, Co. Kildare, Ireland
e-mail: tomas.ward@eeng.nuim.ie

B. Z. Allison et al. (eds.), *Towards Practical Brain-Computer Interfaces*, Biological and Medical Physics, Biomedical Engineering, DOI 10.1007/978-3-642-29746-5_2,
© Springer-Verlag Berlin Heidelberg 2012

modalities produce signals which correlate with neural activation the precise relationships between neural activity and the measured responses are very different [45].

As stated previously many researchers in the BCI community are familiar with the EEG and its underlying neurophysiological origins but the corresponding background to fNIRS is not as widely known. The concept that there is a single vasoactive agent associated with neural activation which in turn causes dilation of the vasculature to increase blood flow is a common misconception for example and a gross oversimplification. The true picture is still being revealed through active research however it is already clear that the process is a complex one [3, 7, 23]. In this section, we briefly summarise the origin of the EEG as commonly measured in a BCI context before presenting a more comprehensive exposition of the agents and events surrounding the haemodynamic response which drives fNIRS.

2.2.1 Origin of the EEG

The EEG represents the electrical potential, usually a difference in potential measured between various points on the scalp. This potential on the scalp arises as a result of neural activity whose action can be considered as a set of distributed current sources embedded in a volume conductor (the head). When the brain is active, patterns of communication are altered across large numbers of neurons, primarily in the form of synaptic state changes. At the cellular level such synaptic activity leads to local changes in the membrane potential which are electrotonically conducted in the form of post-synaptic potentials (PSP). These can be either excitatory (depolarizing) or inhibitory (hyperpolarising) in nature altering the propensity of the neural membrane to generate an action potential [44]. The resultant changes in ionic currents acting through a localised volume conductor constitute what is termed a *local field potential* (LFP). The LFP associated with single cell synaptic activity is very small, however, because of synchronised activation of large numbers of specific sets of neurons in the cortex sharing similar orientation during brain activity, these LFP sum together with their aggregated volume conductor to constitute a substantial current source. Different brain states give rise to different sets of current sources which are unfortunately mixed and filtered as they manifest as biopotentials on the scalp. This makes the reconstruction of the position and geometry of such sources (and hence volumetric localisation of neural activity) an ill-defined inverse problem. The temporal localisation of neural activity is unaffected however and therefore the EEG contains accurate information regarding timing of neural activation patterns.

EEG instrumentation is conceptually simple to understand comprising a sensor and a biopotential difference amplifier. The sensors are called electrodes which converts ionic current flow in the body to electron-based current flow in the amplifier circuitry. As the biopotentials generated on the scalp as a result of neural activity are typically of very low amplitude (10^{-6} V) and extraneous sources of noise sometimes many orders of magnitude greater, good amplifier and electrode system design is key

to producing reliable responses. Consequently the technical development of EEG systems is an active and important field of endeavour [51].

2.2.2 Origin of fNIRS Responses

fNIRS is based on the optical measurement of the haemodynamic response to neural activation [30]. One aspect of this response—the blood oxygen level dependent (BOLD) signal is the basis for functional magnetic resonance imaging (fMRI), a brain imaging modality closely related to fNIRS in terms of the underlying measurand. The responses measuring during fNIRS are usually interpreted in terms of changes in oxy- and deoxyhaemoglobin concentration changes—a somewhat richer set of variables than those available from basic fMRI. As in fMRI, an interpretation of the haemodynamic responses in terms of neural activation is often considered on the simple basis that significant changes in haemodynamics corresponds to increases in neural activation [10]. However, the picture is more complicated that this—indeed much more so and in order to equip neural engineers appropriately for experimentation with this modality and interpretation of data a background on the underlying cellular and even molecular signalling dynamics involved will be presented.

Haemodynamic changes associated with brain activity or more precisely the relationship between local neural activity and cerebral blood flow is termed *neurovascular coupling* [18]. Understanding neurovascular coupling (NVC) is important in terms of interpreting the responses acquired during fNIRS so as to avoid naïve interpretation of the signal. This is especially true in the case of measurement in damaged brain such as following a stroke when pathological conditions of neurovascular mechanisms may exist [29]. Just as it is important to have a basic appreciation of neuronal anatomy and physiology to understand the origin of the EEG a basic understanding of the anatomy of the neurovasculature is useful in understanding the origin of fNIRS responses.

2.2.2.1 Anatomy of the Neurovasculature

The blood supply to the brain (Fig. 2.1a) is carried by extracerebral and intracerebral arteries and arterioles. The main supply to the brain comes from two pairs of cranial arteries; the *internal carotid arteries* (which are bifurcations of the common carotid arteries at the neck) and the *vertebral arteries*. The internal carotid arteries branch at the base of the brain to form two major cerebral arteries; the *anterior cerebral artery* (ACA) and the *middle cerebral arteries* (MCA). The ACA and MCA form the anterior circulation which supplies the *forebrain*. The vertebral arteries consist of a right and left branch which come together to form the *Basilar artery* at the level of the *pons*. This artery then joins up with the internal carotid arteries to form an arterial ring at the base of the brain called the *Circle of Willis*.

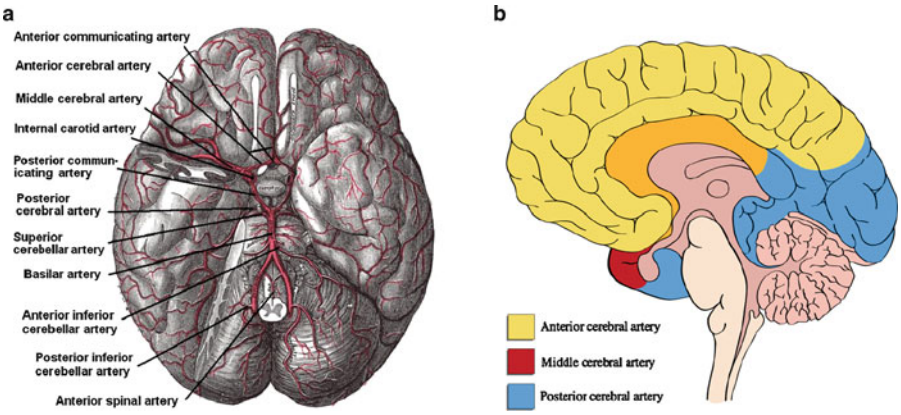

Fig. 2.1 (**a**) Major vessels of the cerebral circulation and (**b**) associated vascular territories

The *posterior cerebral arteries* and two other small arteries called the anterior and posterior communicating arteries also arise at this juncture. The Circle of Willis offers redundancy of circulation between posterior and anterior vasculature systems in the event of blockage in any of the feeding arteries. The posterior cerebral, basilar and vertebral arteries together give rise to the posterior circulation which supplies the posterior cortex. It comprises a number of arterial branches two of which in particular are significant in terms of their vascular territory; the *posterior inferior cerebral artery* and the *anterior inferior cerebral artery*. These arteries supply the *medulla* and pons and their occlusion during a stroke, which is relatively common, leads to specific deficits in somato, sensory and motor function. The vascular territories associated with the various arterial processes are illustrated in Fig. 2.1b.

The posterior and anterior circulation branch into smaller pial arteries and arterioles that branch out over the surface of the brain. These give rise to arterioles which penetrate orthogonally into the brain parenchyma (the functional part of the brain, i.e., neurons and glial cells). These parenchymal arterioles subdivide further into an extensive and distributed capillary network which reflects the metabolic requirements of the underlying neuronal system (Fig. 2.2).

The cerebral vasculature is equipped with neurovascular control mechanisms which match cerebral blood flow (CBF) with local cellular energy needs. These neurovascular coupling mechanisms are distributed and vary in type according to their location along the blood vessel, however the basic regulatory processes arise through interactions between neurons, glia and vascular cells. Neurons and glia in particular produce vaso-dilation or -constriction signals which are in turn transformed into neural activation-matched changes in CBF through the intricately choreographed action of endothelial, pericytes and smooth muscle cells constituting the cerebral vessel walls. The intimate structural and functional relationship between

Fig. 2.2 The cerebral vascular system as revealed through plastic emulsion injection and dissolution of brain parenchyma [53]

cerebral vessels and neural/glial processes involved is significantly important to warrant description with a unique term—the neurovascular unit (NVU). Figure 2.3 illustrates important anatomical aspects of the NVU. At the pial artery stage the tissue consists of an endothelial layer surrounded by smooth muscle cells which in turn is contained in an outer layer (termed adventitia) comprising collagen, fibroblasts and perivascular nerves. Changes in vascular tone at this extracerebral stage are communicated through extrinsic innervation by peripheral nerves originating from cranial autonomic ganglia. As the vessel progresses as a parenchymal arteriole (an intracerebral microvessel) they become progressively smaller and changes in tone are communicated increasingly by local interneurons, glial cells and more centralised forms of intrinsic innervation. Finally as the vessel further penetrates deeper into the parenchyma it loses the smooth muscle layers and branches into cerebral capillaries. These capillaries comprise endothelial cells, contractile cells called pericytes and basal lamina upon which astrocytes (the most common type of glia cell) are attached via specialised processes called "feet." The interface between the walls of capillaries and the surrounding tissue is a very important one as it keeps vascular and extravascular concentrations of ions and molecules at appropriate levels in their respective regions. In the brain, this interface is especially tight and is termed *the blood-brain barrier*.

2.2.2.2 Physiology of the Neurovasculature

NVC dynamics drive the responses measured during fNIRS and act through the anatomical structures identified in the previous section. The role of NVC mechanisms are to provide autoregulation and functional hyperaemia in the brain.

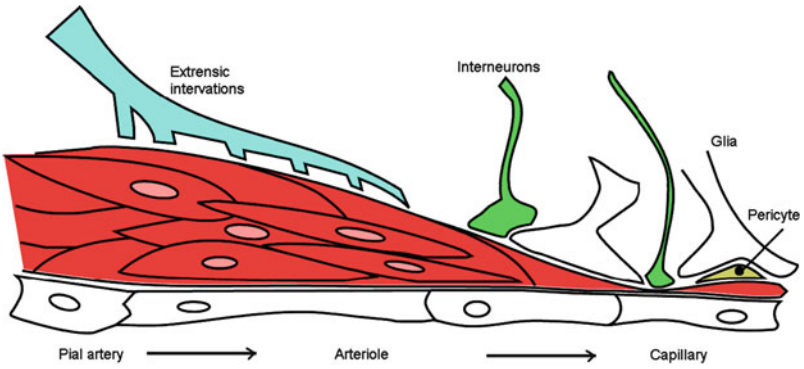

Fig. 2.3 Anatomy of the neurovascular unit (NVU)

Functional hyperaemia is a term which describes increased blood flow associated with increased activation of tissue while autoregulation in this context describes the ability of the cerebral vasculature to maintain the necessary homeostatic blood pressure during periods of changing blood flow. The science of NVC [39] is an active area with a long history [42] and in this article we can only summarise the current understanding of the anatomical and physiological processes involved. Regardless, what is known is that NVC can be understood as a dynamical system comprising sensing apparatus and actuating apparatus. The actuating apparatus act either to relax the vessel (which, all other factors being equal, should increase CBF) in a process termed vasodilation or to constrict the vessel (reducing CBF) in a process called vasoconstriction. These agonistic and antagonistic forces are responsible for generating the appropriate blood flow conditions required for optimal metabolic functioning of the neuronal networks served. Taking the view of Kleinfeld and his colleagues [23], we can group the mechanisms involved as one global and two local pathways. The global pathway is essentially driven through the vasodilatory substance acetylcholine (ACh) and the vasoconstrictor serotonin (5HT) released from various subcortical nuclei in response to blood oxygenation level, cortical state and perhaps even breathing patterns. Of the local pathways one comprises the action of different local interneurons which directly act on the smooth muscle wall of the vessel to produce dilation (through the production of nitric oxide or vasoactive intestinal peptide) or constriction effects (through the production of somatostatin and neuropeptide Y). To complicate matters further some interneurons appear to be capable of releasing both vasodilationary and vasoconstrictive substances. The second local pathway is provided through astrocytes in response to the activity of excitatory neurons [41]. The excitatory neurotransmitter involved is glutamate, the volume conduction of which causes an increase in intracellular levels of Ca^{2+} in astrocytes [35]. During periods of high synaptic activity waves of Ca^{2+} are propagated to nearby blood vessels which are critical in astrocyte-induced vasodilation. It also appears that these changes in

levels of Ca^{2+} trigger the conversion of arachidonic acid to the vasoconstrictor 20-hydroxyeicosatetraenoic (20-HETE) and the dilatory substances prostaglandin E(PG_E) and epoxyeicosatrienoic acid (EET). The relative balance in levels of these substances is a function of the partial pressure of oxygen. Low pO_2 leads to predominately vasodilatory conditions [19].

Even the picture above is a simplification of the processes at work and many new observations and hypothesis are being generated at the time of writing. For example, distinctions are now being highlighted between remote and local vasodilatory mechanisms [36]. The pial arteries which are the primary source of vascular resistance must also undergo dilation/constriction activity in response to downstream activity. Furthermore these adjustments result in increased flow to active areas and reduced flow to nearby inactive areas. The mechanisms driving these upstream activations are still being researched although it appears that signalling along the vessel wall via smooth muscle cells and endothelium is responsible in part. Finally it would appear that under certain conditions stimulus-induced *vasoconstriction* can occur at the site of neural activity [6]. The physiological significance of such behaviour has not yet been elucidated. And finally, results are emerging to suggest that bi-directional information flow is occurring at the vessel-parachyma boundary which has led to speculation that vessel-to-neuron and vessel-to-glial signalling may have a role for information processing in the brain [33].

In summary, what is certain is that there is no single vasoactive agent which simply diffuses through to the capillary beds feeding active neurons to produce the required functional hyperaemia. The emerging understanding is that there is a whole host of vasoactive substances released during neural activation via neurons and glial cells [52] which act on cerebral endothelial cells, pericytes and smooth muscle cells at different levels of the vasculature to produce a coordinated haemodynamic response which results in the appropriate increase in CBF for the active brain area. The interpretation of haemodynamic responses then, in this context of neural activation should therefore be considered carefully as the processes involved are revealing themselves to be increasingly complex and elaborate.

2.2.2.3 The fNIRS Signal

fNIRS measures the haemodynamic response associated with neural activation acting through the mechanisms above. Neural activation essentially causes an increase in glucose and oxygen consumption which in turn through NVC processes cause an increase in cerebral blood flow (CBF) [34]. While the increases in the cerebral metabolic rate of glucose (CMRglu) are matched by the increases in CBF the $CMRO_2$ is much less [14] leading to a net increase in the concentration of oxyhaemoglobin [HbO] with a corresponding change in concentration of deoxyhaemoglobin [Hb]. Figure 2.4 illustrates these changes in the relative states of haemoglobin along with the time course of the concentration changes which can be termed the *haemodynamic response (HR)*. The HR to specific

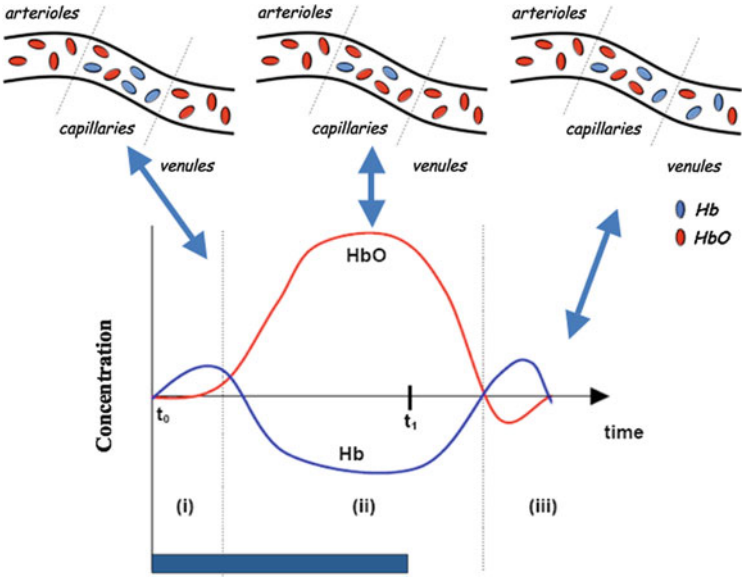

Fig. 2.4 Changes in [HbO][Hb] associated with neural (**a**) early increase in [Hb] (**b**) increase in CBF resulting in increase in [HbO], decrease in [Hb] and (**c**) return to basal state

endogenous/exogenous stimuli is the signal of interest measured with fNIRS. fNIRS in fact measures the optical properties of tissue and its changes in the spectral range of 700–900 nm [21]. This is the near infrared band. Photons of these wavelengths can penetrate the scalp, skull and meninges surrounding the brain to interrogate the superficial layers of the cerebral cortex. Such tissue constitutes a highly scattering medium and consequently backscattered photons can be collected from a detector positioned appropriately on the surface of the scalp to yield information on optical property changes at the cortical level.

The principal optical absorbers (termed *chromophores*) which undergo changes in concentration during neural activation are, conveniently, oxy- and deoxyhaemoglobin. Figure 2.5 illustrates the various types of photon–tissue interaction events which are all highly scattering. For a given photonic flux I_0 only a very small set will arrive at a detector situated a distance L from the optical source. The set of paths taken by photons which are collected at the detector have a geometry which has been described as an "optical banana" [32]. Such a set of photon paths is illustrated in the inset of Fig. 2.5. It is clear from this image which is the output of a Monte Carlo simulation of photon–tissue interaction that the mean path length is L' where $L' > L$. A factor called the differential pathlength factor B, which has been derived experimentally for different tissues, is used to account for this extended pathlength. Therefore $L' = B \cdot L$ is used for subsequent spectroscopic calculations which rely on the mean pathlength. One such calculation which is of great importance in near infrared spectroscopy is the modified Beer–Lambert Law

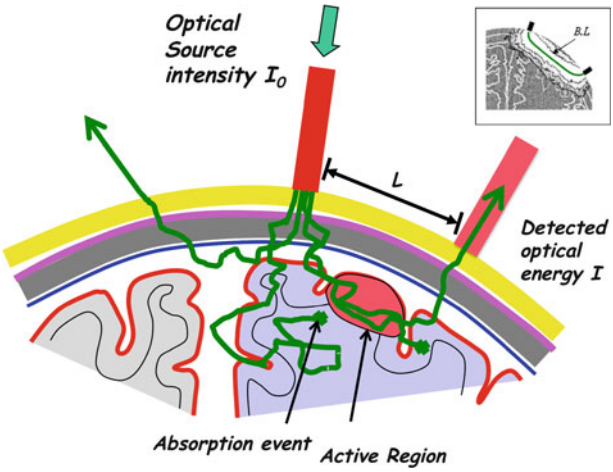

Fig. 2.5 Photon interactions in the head as measured non-invasively from scalp mounted source and detectors

(MBLL). The MBLL relates chromophore concentration levels to optical absorption values. The MBLL can be expressed in terms of the parameters pertinent to fNIRS as follows

$$A_\lambda = \log\left(\frac{1}{T}\right) = (\alpha_{\lambda,Hb} \cdot [Hb] + \alpha_{\lambda,HbO} \cdot [HbO]) \cdot B_\lambda \cdot L + G \tag{2.1}$$

where T is the *transmittance,* which is the ratio of incident power to transmitted power, i.e. $\frac{I_\lambda}{I_{0,\lambda}}$.

The term A_λ is termed the *optical density* and is wavelength specific. The wavelength dependency comes from the wavelength-specific absorption tendencies (represented by the specific extinction coefficients $\alpha_{\lambda,Hb}, \alpha_{\lambda,HbO}$.) of oxy- and deoxyhaemoglobin. These values have been experimentally derived and tabulated elsewhere [9]. The term G is used to account for optical losses dues to scattering and is assumed constant over the measurement period. Usually a differencing operation is used to eliminate the effect of scattering to yield,

$$\Delta A_\lambda = (\alpha_{\lambda,Hb} \cdot .\Delta[Hb] + \alpha_{\lambda,HbO} \cdot \Delta[HbO]) \cdot B_\lambda \cdot L \tag{2.2}$$

and therefore *changes* in chromophore concentrations are a common measurement made during fNIRS studies. In order to resolve the separate contributions of $\Delta[Hb]$ and $\Delta[HbO]$ a number of wavelengths of light are used to yield a set of simultaneous equations which are solved to yield the individual chromophore concentration changes.

The conversion of raw optical density signals to measures of [HbO] and [Hb] proceeds as follows. In this example the optical brain computer interfacing technology

described by [11] is the source of the optical density measurements. This basic continuous wave system uses light emitting diodes rather than lasers as an optical source. The detectors are avalanche photodiodes (APD)-Hammamatsu C5460–01 which are used in many commercial systems. The wavelengths used in this case were 760 nm and 880 nm. Consequently Eq. (2.3) expresses the relationships between the optical variables as follows:

$$\frac{\Delta A_{760\,\mathrm{nm}}}{B_{760\,\mathrm{nm}} \cdot L} = (\alpha_{760\,\mathrm{nm},Hb} \cdot \Delta[Hb] + \alpha_{760\,\mathrm{nm},HbO} \cdot \Delta[HbO]) \tag{2.3}$$

$$\frac{\Delta A_{880\,\mathrm{nm}}}{B_{880\,\mathrm{nm}} \cdot L} = (\alpha_{880\,\mathrm{nm},Hb} \cdot \Delta[Hb] + \alpha_{880\,\mathrm{nm},HbO} \cdot \Delta[HbO]) \tag{2.4}$$

In matrix form these can be expressed as

$$\mathbf{A}/BL = \boldsymbol{\alpha}\mathbf{C} \tag{2.5}$$

where

$$\mathbf{A} = \begin{pmatrix} \Delta A_{760\,\mathrm{nm}} \\ \Delta A_{880\,\mathrm{nm}} \end{pmatrix}, \boldsymbol{\alpha} = \begin{pmatrix} \alpha_{760\,\mathrm{nm},Hb} & \alpha_{760\,\mathrm{nm},HbO} \\ \alpha_{880\,\mathrm{nm},Hb} & \alpha_{880\,\mathrm{nm},HbO} \end{pmatrix} \text{ and } \mathbf{C} = (\Delta[Hb] \quad \Delta[HbO])$$

Equation (2.5) is solved to extract **C** for each time sample as

$$\mathbf{C} = \boldsymbol{\alpha}^{-1} \cdot \mathbf{A}/B \cdot L. \tag{2.6}$$

The differential path length factor is age-dependent as well as altering with wavelength and has been described as follows:

$$B_{780} = 5.13 + 0.07A_y^{0.81} \tag{2.7}$$

A_y is the age of the subject in years and B_{780} is the differential path length factor for 780 nm [9]. Values for other wavelengths can be derived from this measure through a tabulated scaling parameter B_N [9]. Equation (2.6) can be applied at each time step to yield the temporal dynamics of [HbO] and [Hb]. Figure 2.6 shows the results of this calculation for a simple finger tapping exercise lasting 20 s per trial using the system described above. A single source and detector were used measuring over the C3 position (using the 10–20 EEG electrode placement standard). The parameters values used are summarised in Table 2.1.

Figure 2.6 shows the response of 6 trials. The detected light signals were linearly de-trended and low-pass filtered using a fourth order Butterworth filter with a cut-off frequency of 0.5 Hz to remove the cardiac pulsations. A clear elevation in [HbO] levels is apparent as well as a reduction in [Hb]. There is a considerable lag in the

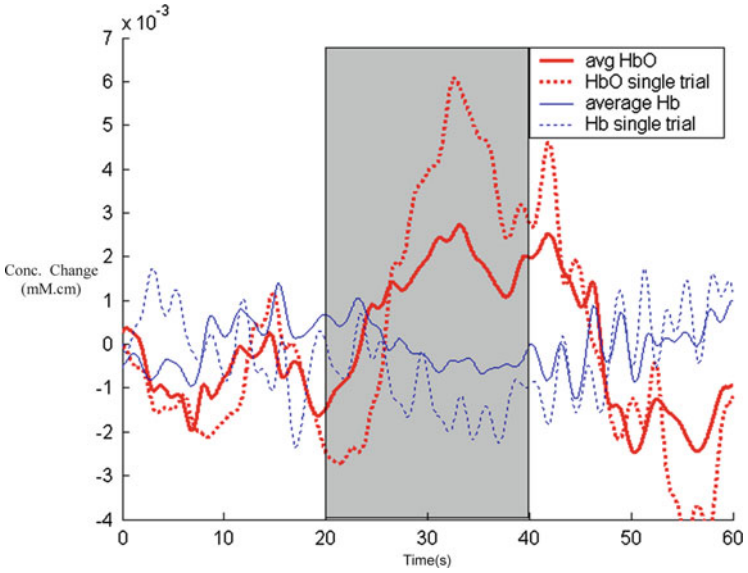

Fig. 2.6 [HbO] and [Hb] changes during a motor task (*shaded area*) illustrating average and single trial responses over the *left hand side* primary motor cortex

Table 2.1 Values of parameters used to calculate NIRS response in Fig. 2.6

Wavelength (nm)	HbO–Extinction Co-efficient ($mM^{-1}cm^{-1}$)	Hb–Extinction Co-efficient ($mM^{-1}cm^{-1}$)	B_N
760	0.6096	1.6745	1.12
880	1.2846	0.3199	0.84

haemodynamic response of about 6–8 s which of course has implications for use in brain computer interfacing applications.

The fNIRS responses in Fig. 2.6 are stereotypical for the modality and clearly demonstrate the evolution of the temporal responses. When measured using a number of source-detector pairs over the scalp and processed through an appropriate tomographic algorithm images of brain activation over cortical areas can be derived [2]. Such images provide the spatial localisation capability which are of utility for increasing the bit rate when used as a BCI [46] or for more general studies of brain function [1, 28]. For the purposes of clarity and simplicity, however, the remainder of this chapter considers only the temporal aspects of fNIRS, as it is only that aspect which has been incorporated in the fNIRS-EEG systems discussed later. In the next section time domain models for fNIRS responses are given which both helps reveal the signal processing problems inherent in the modality and provides a basis for understanding the response vis-a-vis the EEG.

2.3 Signal Models

Recently data has emerged which is leading to a better understanding of the relationships between fNIRS data and the EEG. Blankertz in particular has proposed that EEG activity leads to a damping in haemodynamics. This line of research is important and will ultimately, one would hope, lead to the required bridging subcomponents which will provide a unified fNIRS-EEG signal model. Currently such observations have not however been transformed into a model which lends itself to improving signal extraction for fNIRS-EEG systems. In this section then some of the basic building blocks which might be useful for the development of such signal-oriented models are presented with an emphasis on fNIRS systems. Signal models for the EEG are highly dependent on the neurophysiological origin of the underlying active components, however for many BCI applications the EEG can be interpreted as a series of synchronisation and desynchronisation events across a relatively small set of frequency bands. Models based on phase modulation (and even shifting) of these bands are a suitable conceptual model in many cases. The optical haemodynamic response is more straightforward and brain activation can be considered simply as the aggregation of active "voxels" not unlike fMRI. Simple as it may be, signal models which may be of practical utility to neural engineers interested in the processing of these responses are only beginning to emerge. Full dynamical system representations of the underlying haemodynamic responses have been developed, however, these models are not easy to work with and a simpler model is presented here which captures many aspects of the signal including all relevant components of extrinsic and physiological origin. This model is used to illustrate the effect of various parameters on signal characteristics and is a useful explanatory tool. This model comprises both a tractable physiological model of the neurovascular coupling events and a spectrophotometric model which captures the effect of the sensor apparatus in converting these neurovascular dynamics to changes in signal levels in the optical detectors based on Eq. (2.1). The model is expanded to include a number of extraneous noise sources normally presented during real fNIRS studies such as cardiac pulsations, respiration and other fluctuations in blood pressure which given rise to haemodynamic changes.

2.3.1 Modelling the Vascular Response

Several models have been proposed to account for the changes in blood volume, flow, oxy- and deoxyhaemoglobin concentrations which characterise the haemodynamic signal associated with neural activation. Of these, the best known and most widely invoked are the Windkessel-based models of Mandeville and his colleagues [31] and the balloon model of Buxton [5]. Both of these biomechanical models attempt to capture the dynamic changes in the post arteriole vasculature as a function of neural stimulus. Here, we utilise the balloon model which makes the assumption that the vascular bed which constitutes cerebral blood volume (CBV)

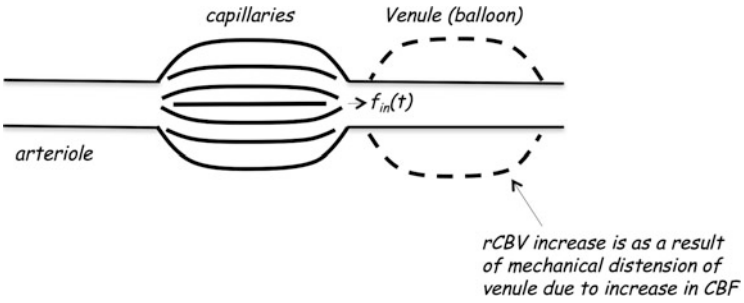

Fig. 2.7 The balloon model of the neurovascular response relating neural activation to changes in cerebral blood volume

can be modelled to some extent as an expandable venous compartment (hence the term "balloon"). The expansion of this balloon is driven by CBF which is assumed to be directly proportional to neural activation (Fig. 2.7).

A key part of the model then is the outflow from this vascular compartment which is a function of the compartmental volume. The precise form of this blood volume function governs the haemodynamics generated, and in the original exposition of this work Buxton and his colleagues show a number of different examples of this dependency. Generally the model is an appropriate balance between simplicity of representation and explanatory physiological power. It captures many of the well known aspects of the HRF as measured during fMRI such as transient changes in deoxyhaemoglobin and oxy-haemoglobin concentrations as well as the initial dip and other peculiarities of the BOLD response as measured experimentally.

The differential equation form of the model is as follows:

$$E(t) = 1 - (1 - E_0)^{\frac{1}{f_{in}(t)}} \tag{2.8}$$

$$\dot{q}(t) = \frac{f_{in}(t)}{\tau_0}\left[\frac{E(t)}{E_0} - \frac{q(t)}{v(t)}\right] + \frac{1}{\tau_v}\left[f_{in}(t) - v^{\frac{1}{\alpha}}\right]\frac{q(t)}{v(t)} \tag{2.9}$$

$$\dot{v}(t) = \frac{1}{\tau_v}\left[f_{in}(t) - v^{\frac{1}{\alpha}}\right] \tag{2.10}$$

$$\dot{p}(t) = \frac{1}{\tau_v}\left[f_{in}(t) - v^{\frac{1}{\alpha}}\right]\frac{p(t)}{v(t)} \tag{2.11}$$

E, q, v and p represent oxygen extraction rate, normalised [Hb], normalised blood volume and normalised total haemoglobin concentration respectively. [HbO] is obtained by subtracting q from p. Neural activation is represented by the CBF function $f_{in}(t)$ and is usually modelled as a binary function representing the stimulus input.

Figure 2.8 shows a solution for the Eqs. (2.8)–(2.11) for a trapezoidal binary input for f_{in}. This corresponds to a binary neural activation event. The output of the model displays the canonical form for the haemodynamic response to neural

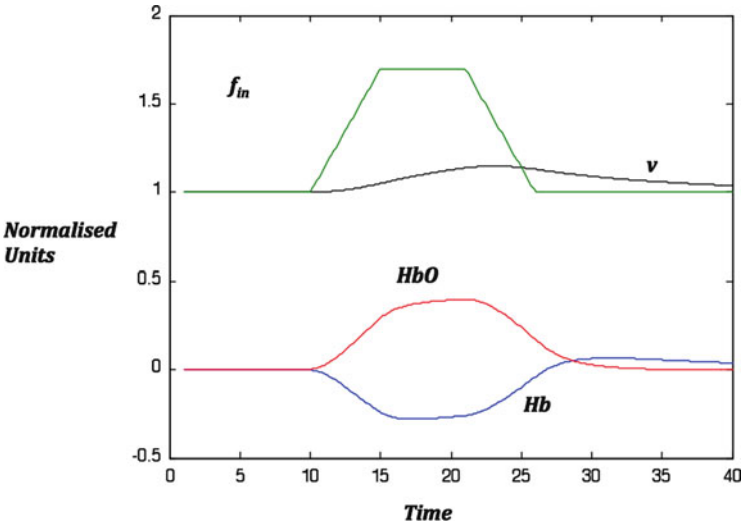

Fig. 2.8 The balloon model of the neurovascular response relating neural activation to changes in CBV. From *top* to *bottom* the variables plotted are CBF, normalised blood volume, [HbO] and [Hb]

activation. The model above has been used previously to generate a priori estimate for the BOLD response to specific stimuli patterns. A similar approach can be taken with fNIRS using such a model for predicting [HbO] and [Hb] changes for a given stimulus [13].

2.3.2 Spectrophotometric Translation

In fMRI the measured BOLD response is derived from the balloon model through known relationships between the relative contributions of the magnetic susceptibilities involved for oxy- and deoxyhaemoglobin and the signal measured at the detection apparatus. In contrast, fNIRS is an optical measurement and therefore it is changes in the optical properties of the tissue volume during neural activation that induces signal changes. Consequently a spectrophotometric modelling component is required to capture this aspect of the signal. The signal acquired at the detector can be approximated as a linear mixture of a number of components [27]. The basic equation involved is the MBLL in Eq. (2.1) however this equation must be altered to account for additional sources of optical density changes due to other sources of physiological origin especially low frequency blood pressure oscillations (Mayer wave), scattering and absorption changes due to the cardiac cycle and respiration [12]. A basic representation is as follows

$$S(\lambda, t) = \varphi_b(\lambda, t) + \varphi_c(\lambda, t) + \varphi_m(\lambda, t) + \varphi_n(\lambda, t) \tag{2.12}$$

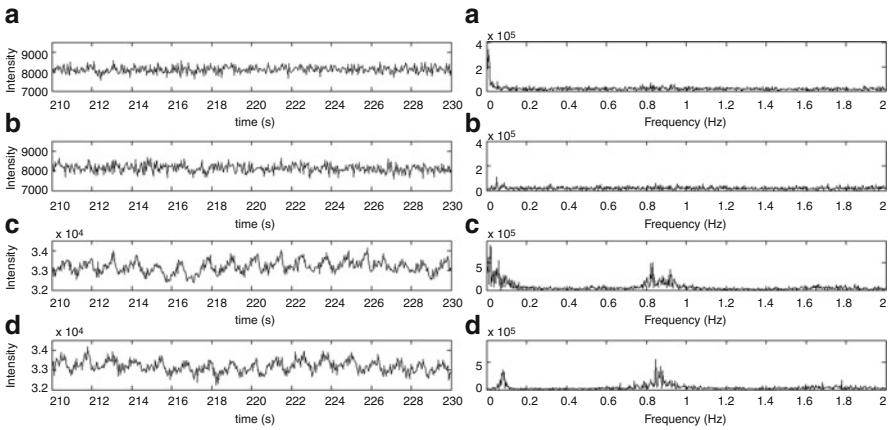

Fig. 2.9 Visual comparison of synthetic fNIRS model with real optical density signals. The *left hand side* is the time domain while the corresponding spectra are on the *right hand side*. (**a**) Actual measurement at 690 nm, (**b**) synthetic output for 690 nm, (**c**) actual measurement at 830 nm and (**d**) synthetic output at 830 nm

where

$$\varphi_b(\lambda, t) = e^{\Delta A_\lambda} \tag{2.13}$$

$$\varphi_c(\lambda, t) = K(\lambda) \cdot f(k(t), R(t)) \tag{2.14}$$

$$\varphi_m(\lambda, t) = M(\lambda) \cdot \sin(2 \cdot \pi \cdot f_m \cdot t + \theta) \tag{2.15}$$

Equation (2.13) represents the transmittance as given by Eq. (2.2) driven by the [HbO] and [Hb] values predicted by Eqs. (2.8) through (2.11). Equation (2.14) represents transmittance changes associated with the cardiac cycle and in this instance is a wavelength dependent scaling of a piecewise linear cardiac pulse $k(t)$ which is temporally scaled according to the rate function $R(t)$. The Mayer wave is represented in Eq. (2.15) as a sinusoidal component at frequency f_m whose amplitude is a function of wavelength. The term $\varphi_n(\lambda, t)$ accounts for optical environmental noise sources and can be adequately represented by a normally distributed noise signal.

2.3.3 Synthetic Signal Generation

Simulation of (2.12) with appropriately tuned parameters can yield realistic optical signals. The neural activation is incorporated through the cerebral blood flow signal as described in Sect. 2.2.2.3. Figure 2.9 shows sample output from this model along with real fNIRS signals both in the time and frequency domain. It is apparent that the model captures many of the characteristic features of the signal in both domains.

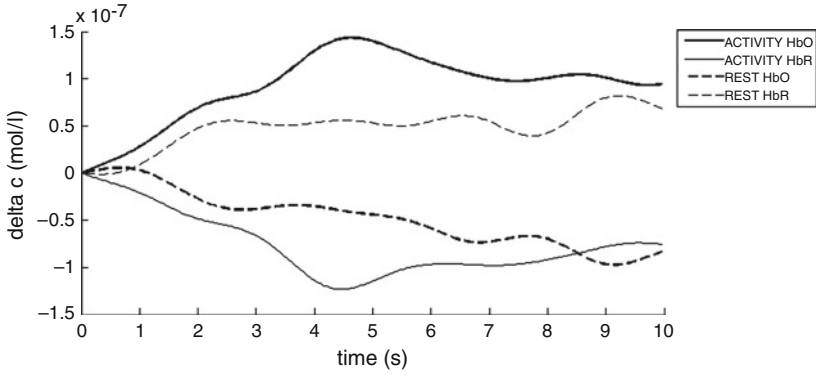

Fig. 2.10 Averaged derived changes in [HbO] and [Hb] responses both at rest and in response to activation using the synthetic signal model (compare with Fig. 2.6)

The output of such a model can be put through the same signal processing pipeline as actual fNIRS data to yield responses such as $\Delta[Hb]$ and $\Delta[HbO]$. Figure 2.10 illustrates the results of this processing for the synthetic data above in which $f_{in}(t)$ was modelled as a trapezoid with a rise time of 5 s, plateau time of 5 s, fall time of 5 s, and a rest time of 5 s. The amplitude of $f_{in}(t)$ was 1.7 units for a 10 s active period followed by a 10 s rest period. This was then repeated to match the number of active and rest periods of the real fNIRS data (there were 20 such periods in this case) and the responses averaged [27].

The most useful feature of this model for synthetic fNIRS data generation is the flexibility afforded when constructing the data. All parameters can be fine-tuned to replicate a real fNIRS signal. Such a signal model is useful for signal processing research as it allows a systematic investigation of the effect of various parameters on the fNIRS recording process. For example, the effect of movement artefact can be examined through varying the L parameter in Eq. (2.6) during the measurement simulation. Although fNIRS systems are a lot less sensitive to movement than fMRI, this type of artefact can cause problems and methods for motion artefact removal are an active research area [16, 47, 48].

The above section provides a sketch for a number of practical approaches to modelling the fNIRS signal. Such ideas can be combined with basic EEG models to yield a compound model encompassing both modalities. The neural activation function $f_{in}(t)$ is clearly the nexus between the two models and emerging research especially in the EEG-fMRI domain will elucidate more precisely the coupling mechanisms involved [22, 24, 43]. Even in the absence of comprehensive models it is clear that fNIRS and EEG are each measuring some aspects of neural activation [25, 40] and in the next section we summarise some early results we have obtained through combining the modalities for brain computer interfacing-like applications.

2.4 Combined EEG-fNIRS Measurements in Overt and Imagined Movement Tasks

To demonstrate the utility of combining the fNIRS and EEG modalities a pair of experiments are described. Both experiments involve the monitoring of motor cortex however in the first experiment the task involves overt finger tapping while the second experiment involves imagined movement only. The EEG processing is based on a standard motor rhythm paradigm—Event Related Synchronisation/Desynchronisation (ERS/ERD), which is a relative increase/decrease in the band power of a chosen frequency range that coincides with some event [37]. In ERS/ERD analysis, a baseline "reference" period of EEG data is recorded before the event and then compared to an "activity" period of EEG data, recorded during or following the event. ERD is known to occur in the μ frequency range (8–12 Hz) on movement onset and ERS is known to occur in the β frequency range (12–30 Hz) following movement offset.

2.4.1 fNIRS/EEG Sensor

A hybrid probe was designed to hold three fNIRS light sources (laser diodes), three fNIRS light detectors (APDs) and seven EEG electrodes in the array shown in Fig. 2.11 [26]. There are seven fNIRS channels with the corresponding EEG electrodes located directly above the centre point of each fNIRS channel. The centre point of an fNIRS channel is the interrogated area of cortex (as in Fig. 2.5), so with this set-up, we are recording electrical and haemodynamic activity from approximately the same area of cortex. An alternate combination probe is to include the electrode as part of the optical fibre housing however such a design is more complex to fabricate [8, 49]. Thus, we have seven co-locational, dual-modality recording sites. fNIRS data was recorded using a TechEn CW6 system (TechEn Inc., USA). Wavelengths used were 690 nm and 830 nm, sampled at 25 Hz. EEG data was recorded using a BioSemi Active-Two system (BioSemi Inc., The Netherlands) at 2,048 samples/s.

2.4.2 Experimental Description

In this simple proof-of-concept experiment data was collected from two healthy individuals. Both subjects gave voluntary consent. Subject A was male, 37 years old and left-handed (self-reported). Subject B was male, 26 years old and right-handed (self reported). During the experiment, the subjects were seated in a comfortable chair viewing a computer screen which presented instructions. Subjects were instructed to tap each of their fingers to their thumb on both hands. Tapping was self-paced. Individual trials lasted for 20 s, during which time the on-screen instruction read either "TAP" (an "active" trial) or "RELAX" (a "rest" trial). Twenty trials were

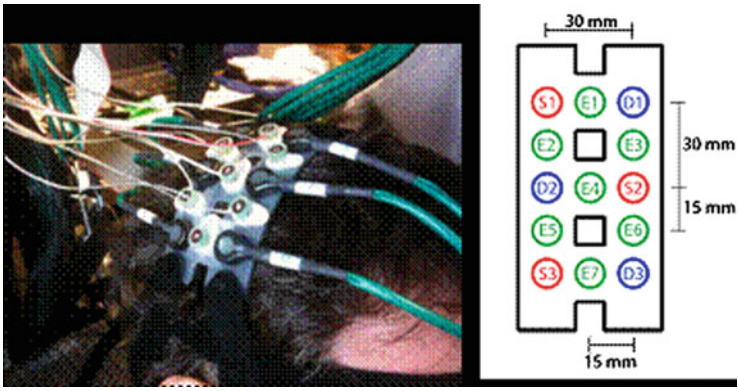

Fig. 2.11 fNIRS/EEG probe used in the experiments. SX, DX and EX denote source, detector and electrode positions respectively

carried out per experimental run, which alternated between active and rest, lasting 400 s in total. Two experimental runs were recorded for each subject with a short break between runs. The central electrode of the fNIRS/EEG recording module was located at C3 for Subject A (left-handed) and C4 for Subject B (right-handed). In a second series of experiments the above was repeated however rather than overt movement subjects were asked to perform imagined movement tasks.

2.4.3 Signal Processing

EEG data was first analysed to identify the frequencies at which ERS and ERD occurred in the μ frequency range and β frequency range with respect to the transition events, i.e., the transition from rest to active periods and vice-versa. The frequency ranges at which ERS and ERD occurred were identified through inspection of spectral plots for the reference and activity periods during both events. Raw EEG data was bandpass filtered with a sixth-order Butterworth filter to the identified ERS/ERD ranges, squared to obtain a power signal and then smoothed using a lowpass sixth-order Butterworth filter at 5 Hz. For ERS/ERD analysis, the reference window was chosen to be between 4.5 and 3.5 s before both types of event. For a transition from a rest trial to an active trial, the activity window was selected to be from 0 to 1 s after the transition. For a transition from active to rest, the activity window was selected to be from 0.5 to 1.5 s after the transition. These windows were chosen to capture the expected timing of pre-movement μ-rhythm ERD and β post-movement ERS. These changes in μ and β power were used as features for EEG classification. For fNIRS, the 690 nm and 830 nm raw intensity measurements were processed according to the techniques described in Sect. 2.2. The amplitude of these responses were used as features for motor cortical activation detection.

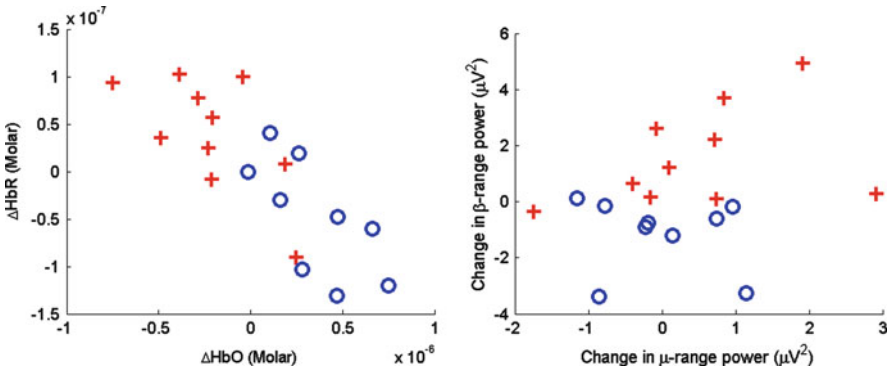

Fig. 2.12 *Left hand side*, 2D fNIRS feature space for Channel 2 of Subject A, Trial 1. *Crosses* indicate feature locations when subject is in a rest period. *Circles* indicate feature locations when subject is in a finger-tapping period. *Right hand side*, 2D EEG feature space for Channel 2 of Subject A, Trial 1

Classification was performed on the fNIRS and EEG signals to classify the activity into one of two classes: "active" and "rest." We employed the Linear Discriminant Analysis (LDA) classifier and calculated classification accuracy via leave-one-out cross-validation (LOOCV). In particular, for N trials, $N-1$ trials were used for training the classifier and the remaining trial was used for testing. This was repeated N times with each trial used for testing once. Classification accuracy was calculated as the number of correct classifications over N.

For EEG, the feature extracted was change in μ-rhythm and β-rhythm power from the reference period to the activity period at the beginning of a trial. This resulted in a two-dimensional EEG feature space (Fig. 2.12). For fNIRS, the average change in amplitude of the $\Delta[HbO]$ and $\Delta[Hb]$ signals over a trial were used to define a two-dimensional fNIRS feature space. By combining the fNIRS and EEG feature spaces, an fNIRS/EEG four-dimensional feature space was also created for classification.

2.4.4 Results

A table of classification results are presented in Tables 2.2 and 2.3. Shown is the classification accuracy of the classifier when operating on fNIRS features only, EEG features only and the combined feature space. The results show that utilising both fNIRS and EEG features for classification yields an improvement on classification accuracy.

The classification accuracy particularly for imagined movement is not particularly impressive, however, there was no subject training for such imagined movement. More importantly the goal of the above experiments is not to demonstrate

Table 2.2 Classification accuracy for overt movement tasks

	Subject A						Subject B					
	Trial 1			Trial 2			Trial 1			Trial 2		
Channel	fNIRS (%)	EEG (%)	Comb. (%)	fNIRS (%)	EEG (%)	Comb. (%)	fNIRS (%)	EEG (%)	Comb. (%)	fNIRS (%)	EEG (%)	Comb. (%)
1	84	79	90	100	84	95	79	84	95	79	84	84
2	79	79	84	95	79	95	47	79	63	53	84	84
3	100	74	95	100	84	100	79	74	79	84	84	84
4	95	84	95	84	84	79	74	74	63	53	90	79
5	74	74	84	42	74	58	47	68	47	74	79	95
6	100	90	100	95	74	90	58	74	68	79	84	79
7	58	84	84	68	68	79	68	63	68	58	74	63
Average	84	80	90	83	78	85	65	74	69	68	83	81

Table 2.3 Classification accuracy for imagined movement tasks

	Subject A			Subject B		
Channel	fNIRS (%)	EEG (%)	Dual (%)	fNIRS (%)	EEG (%)	Dual (%)
1	59	51	64	64	46	62
2	56	59	67	51	54	59
3	56	54	64	61	41	56
4	69	67	72	64	59	67
5	61	51	72	41	36	46
6	56	77	64	74	59	69
7	56	59	62	15	43	49
Average	59	60	66	53	48	58

a high performance imagined movement task-based BCI operation but to illustrate how a combined EEG/fNIRS probe can work to yield both electrical and haemodynamic signatures of motor cortical activation which results in a higher information carrying compound signal. The features used are only of a rudimentary nature and it is likely that there is significant additional information regarding cortical function residing in this combined signal space. Indeed, the hybrid signal produced is a measure of neurovascular coupling and could have enhanced value when measured for subjects who have suffered stroke or similar cerebro-vascular damage. Fusion approaches such as the above are part of the next phase of BCI development [4, 17, 20] which will require enhanced, robust performance outside the laboratory setting.

2.5 Conclusion

In this chapter we have provided a description of EEG-fNIRS hybrid neural-haemodynamic technology for basic brain computer interfacing applications. The primary contributions has been an introduction to the neurovascular response which bridges neural activity and the haemodynamic response, the presentation of a synthetic signal model which facilitates a better understanding of the fNIRS signal especially for signal processing engineers, and the presentation of a set of results demonstrating how a compound EEG-fNIRS probe can yield a neural interfacing technology with a superior capacity to accurately monitor motor cortical activations.

It is clear that hybrid measurement modalities have great potential in creating the next generation of BCI. The fNIRS-EEG technology discussed here is but one example of such an approach although it is one that might be quite fruitful particularly when used with the damaged brain where measurements of neurovascular coupling may have great diagnostic and ongoing cortical status monitoring capability. The field of compound fNIRS-EEG interface technology is only beginning to develop and we believe that as fNIRS technology improves and becomes less expensive more

ingenious methods for extracting neural activation signatures will be developed leading to more powerful and useful BCI applications.

Acknowledgements This work was supported by Science Foundation Ireland: Research Frontiers Program 2009, Grant No. 09/RFP/ECE2376.

References

1. Arenth, P.M., Ricker, J.H., Schultheis, M.T.: Applications of functional near-infrared spectroscopy (fNIRS) to Neurorehabilitation of cognitive disabilities. Clin. Neuropsychol. **21**(1), 38–57 (2007)
2. Arridge, S.R.: Optical tomography in medical imaging. Inverse Probl. **15**(2), R41–R93 (1999)
3. Bernardinelli, Y., Salmon, C., Jones, E.V., Farmer, W.T., Stellwagen, D., Murai, K.K.: Astrocytes display complex and localized calcium responses to single-neuron stimulation in the hippocampus. J. Neurosci. **31**(24), 8905–8919 (2011)
4. Brunner, P., Bianchi, L., Guger, C., Cincotti, F., Schalk, G.: Current trends in hardware and software for brain–computer interfaces (BCIs). J. Neural Eng. **8**(2), 025001 (2011)
5. Buxton, R.B., Wong, E.C., Frank, L.R.: Dynamics of blood flow and oxygenation changes during brain activation: the balloon model. Magn. Reson. Med. **39**(6), 855–864 (1998)
6. Cauli, B., Tong, X.K., Rancillac, A., Serluca, N., Lambolez, B., Rossier, J., Hamel, E.: Cortical GABA interneurons in neurovascular coupling: relays for subcortical vasoactive pathways. J. Neurosci. **24**(41), 8940–8949 (2004)
7. Cloutier, M., Bolger, F.B., Lowry, J.P., Wellstead, P.: An integrative dynamic model of brain energy metabolism using in vivo neurochemical measurements. J. Comput. Neurosci. **27**(3), 391–414 (2009)
8. Cooper, R.J., Everdell, N.L., Enfield, L.C., Gibson, A.P., Worley, A., Hebden, J.C.: Design and evaluation of a probe for simultaneous EEG and near-infrared imaging of cortical activation. Phys. Med. Biol. **54**(7), 2093–2102 (2009)
9. Cope, M.: The application of near-infrared spectroscopy to non-invasive monitoring of cerebral oxygenation in the newborn infant. PhD thesis, University of London (1991)
10. Coyle, S., Ward, T., Markham, C., McDarby, G.: On the suitability of near-infrared (NIR) systems for next-generation brain–computer interfaces. Physiol. Meas. **25**(4), 815–822 (2004)
11. Coyle, S.M., Ward, T.E., Markham, C.M.: Brain–computer interface using a simplified functional near-infrared spectroscopy system. J. Neural Eng. **4**(3), 219–226 (2007)
12. Coyle, S., Ward, T., Markham, C.: Physiological noise in near-infrared spectroscopy: implications for optical brain computer interfacing. Conf. Proc. IEEE Eng. Med. Biol. Soc. **6**, 4540–4543 (2004)
13. Cui, X., Bray, S., Reiss, A.L.: Functional near infrared spectroscopy (NIRS) signal improvement based on negative correlation between oxygenated and deoxygenated hemoglobin dynamics. Neuroimage. **49**(4), 3039–3046 (2010)
14. Davis, T.L., Kwong, K.K., Weisskoff, R.M., Rosen, B.R.: Calibrated functional MRI: mapping the dynamics of oxidative metabolism. Proc. Natl. Acad. Sci. USA. **95**(4), 1834–1939 (1998)
15. Dobkin, B.H.: Brain–computer interface technology as a tool to augment plasticity and outcomes for neurological rehabilitation. J. Physiol. **579** (Pt 3), 637–642 (2007)
16. Falk, T.H., Guirgis, M., Power, S., Chau, T.T.: Taking NIRS-BCIs outside the lab: towards achieving robustness against environment noise. IEEE Trans. Neural Syst. Rehabil. Eng. **19**(2), 136–146 (2011)
17. Fazli, S., Mehnert, J., Steinbrink, J., Curio, G., Villringer, A., Müller, K.R., Blankertz, B.: Enhanced performance by a hybrid NIRS-EEG brain computer interface. Neuroimage. **59**(1), 519–29 (2011)

18. Filosa, J.A.: Vascular tone and neurovascular coupling: considerations toward an improved in vitro model. Front. Neuroenergetics. **2**(16), 1–8 (2010)
19. Gordon, G.R., Choi, H.B., Rungta, R.L., Ellis-Davies, G.C., MacVicar, B.A.: Brain metabolism dictates the polarity of astrocyte control over arterioles. Nature. **456**(7223), 745–749 (2008)
20. Green, A.M., Kalaska, J.F.: Learning to move machines with the mind. Trends Neurosci. **34**(2), 61–75 (2011)
21. Jöbsis, F.F.: Noninvasive, infrared monitoring of cerebral and myocardial oxygen sufficiency and circulatory parameters. Science **198**(4323), 1264–1267 (1977)
22. Kilner, J.M., Mattout, J., Henson, R., Friston, K.J.: Hemodynamic correlates of EEG: a heuristic. Neuroimage **28**(1), 280–286 (2005)
23. Kleinfeld, D., Blinder, P., Drew, P.J., Driscoll, J.D., Muller, A., Tsai, P.S., Shih, A.Y.: A guide to delineate the logic of neurovascular signaling in the brain. Front. Neuroenergetics. **3**, 1 (2011)
24. Laufs, H., Holt, J.L., Elfont, R., Krams, M., Paul, J.S., Krakow, K., Kleinschmidt, A.: Where the BOLD signal goes when alpha EEG leaves. Neuroimage **31**(4), 1408–1418 (2006)
25. Lauritzen, M., Gold, L.: Brain function and neurophysiological correlates of signals used in functional neuroimaging. J. Neurosci. **23**(10), 3972–3980 (2003)
26. Leamy, D.J., Ward, T.E.: A novel co-locational and concurrent fNIRS/EEG measurement system: design and initial results. Conf. Proc. IEEE Eng. Med. Biol. Soc. **2010**, 4230–4233 (2010)
27. Leamy, D.J., Ward, T.E., Sweeny, K.T.: Functional near infrared spectroscopy (fNIRS) synthetic data generation. Conf. Proc. IEEE Eng. Med. Biol. Soc. 6589–6592 (2011)
28. Leff, D.R., Orihuela-Espina, F., Elwell, C.E., Athanasiou, T., Delpy, D.T., Darzi, A.W., Yang, G.Z.: Assessment of the cerebral cortex during motor task behaviours in adults: A systematic review of functional near infrared spectroscopy (fNIRS) studies. Neuroimage **54**(4), 2922–2936 (2011)
29. Lin, W.H., Hao, Q., Rosengarten, B., Leung, W.H., Wong, K.S.: Impaired neurovascular coupling in ischaemic stroke patients with large or small vessel disease. Eur. J. Neurol. **18**(5), 731–736 (2011)
30. Lloyd-Fox, S., Blasi, A., Elwell, C.E.: Illuminating the developing brain: the past, present and future of functional near infrared spectroscopy. Neurosci. Biobehav. Rev. **34**(3), 269–284 (2010)
31. Mandeville, J.B., Marota, J.J., Ayata, C., Zaharchuk, G., Moskowitz, M.A., Rosen, B.R., Weisskoff, R.M.: Evidence of a cerebrovascular postarteriole windkessel with delayed compliance. J. Cereb. Blood Flow Metab. **19**(6), 679–689 (1999)
32. Mansouri, C., L´huillier, J.P., Kashou, N.H., Humeau, A.: Depth sensitivity analysis of functional near-infrared spectroscopy measurement using three-dimensional Monte Carlo modelling-based magnetic resonance imaging. Lasers Med. Sci. **25**(3), 431–438 (2010)
33. Moore, C.I., Cao, R.: The hemo-neural hypothesis: on the role of blood flow in information processing. J. Neurophysiol. **99**(5), 2035–2047 (2008)
34. Nair, D.G.: About being BOLD. Brain Res. Rev. **50**(2), 229–243 (2005)
35. Panatier, A., Vallée, J., Haber, M., Murai, K.K., Lacaille, J.C., Robitaille, R.: Astrocytes are endogenous regulators of Basal transmission at central synapses. Cell **146**(5), 785–798 (2011)
36. Pelligrino, D.A., Vetri, F., Xu, H.L.: Purinergic mechanisms in gliovascular coupling. Semin. Cell Dev. Biol. **22**(2), 229–236 (2011)
37. Pfurtscheller, G., Lopes da Silva, F.H.: Event-related EEG/MEG synchronization and desynchronization: basic principles. Clin. Neurophysiol. **110**(11), 1842–1857 (1999)
38. Richards, L., Hanson, C., Wellborn, M., Sethi, A.: Driving motor recovery after stroke. Top Stroke Rehabil. **15**(5), 397–411 (2008)
39. Riera, J., Sumiyoshi, A., Brain oscillations. Ideal scenery to understand the neurovascular coupling. Curr. Op. Neurobiol. **23**, 374–381 (2010)
40. Rosa, M.J., Daunizeau, J., Friston, K.J.: EEG-fMRI integration: A critical review of biophysical modeling and data analysis approaches. J. Integr. Neurosci. **9**(4), 453–476 (2010)
41. Rouach, N., Koulakoff, A., Abudara, V., Willecke, K., Giaume, C.: Astroglial metabolic networks sustain hippocampal synaptic transmission. Science **322**(5907), 1551–1555 (2008)

42. Roy, C.S., Sherrington, C.S.: On the regulation of the blood supply of the brain. J. Physiol. **11**, 85–108 (1890)
43. Scheeringa, R., Fries, P., Petersson, K.M., Oostenveld, R., Grothe, I., Norris, D.G., Hagoort, P., Bastiaansen, M.C.: Neuronal dynamics underlying high- and low-frequency EEG oscillations contribute independently to the human BOLD signal. Neuron **69**(3), 572–583 (2011)
44. Schomer, D.L., Lopes da Silva, F.H.: (eds.) Niedermeyer´s Electroencephalography: Basic Principles, Clinical Applications, and Related Fields. 6th Edition, Lippincott, Williams and Wilkins, Philadelphia (Penn.) (2011)
45. Shibasaki, H.: Human brain mapping: hemodynamic response and electrophysiology. Clin. Neurophysiol. **119**(4), 731–743 (2008)
46. Sitaram, R., Caria, A., Birbaumer, N.: Hemodynamic brain–computer interfaces for communication and rehabilitation. Neural Netw. **22**(9), 1320–1328 (2009)
47. Sweeney, K.T., Leamy, D.J., Ward, T.E., McLoone, S.: Intelligent artifact classification for ambulatory physiological signals. Conf. Proc. IEEE Eng. Med. Biol. Soc. **2010**, 6349–6352 (2010)
48. Sweeney, K.T., Ayaz, H., Ward, T.E., Izzetoglu, M., McLoone, S.F., Onaral, B.: A Methodology for Validating Artifact Removal Techniques for fNIRS. Conf. Proc. IEEE Eng. Med. Biol. Soc. 4943–4946 (2011)
49. Wallois, F., Patil, A., Héberlé, C., Grebe, R.: EEG-NIRS in epilepsy in children and neonates. Neurophysiol. Clin. **40**(5–6), 281–292 (2010)
50. Ward, T.E., Soraghan, C.J., Matthews, F., Markham, C.: A concept for extending the applicability of constraint-induced movement therapy through motor cortex activity feedback using a neural prosthesis. Comput. Intell. Neurosci. 51363 (2007)
51. Webster, J.G. (eds.): Medical Instrumentation, Application and Design, 3rd edn. Wiley, Hoboken, N.J. (1998)
52. Zonta, M., Angulo, M.C., Gobbo, S., Rosengarten, B., Hossmann, K.A., Pozzan, T., Carmignoto, G.: Neuron-to-astrocyte signaling is central to the dynamic control of brain microcirculation. Nat. Neurosci. **6**(1), 43–50 (2003)
53. Zlokovic, B., Apuzzo, M.: Strategies to circumvent vascular barriers of the central nervous system. Neurosurgery **43**, 877–878 (1998)

Springer

http://www.springer.com/978-3-642-29745-8

Towards Practical Brain-Computer Interfaces
Bridging the Gap from Research to Real-World Applications

Allison, B.; Dunne, S.; Leeb, R.; Del R. Millán, J.; Nijholt, A. (Eds.)

2013, XXIV, 412 p., Hardcover
ISBN: 978-3-642-29745-8